



## Finite ballooning angle effects on ion temperature gradient driven mode in gyrokinetic flux tube simulations

Rameswar Singh, S. Brunner, R. Ganesh, and F. Jenko

Citation: *Physics of Plasmas* (1994-present) **21**, 032115 (2014); doi: 10.1063/1.4868425

View online: <http://dx.doi.org/10.1063/1.4868425>

View Table of Contents: <http://scitation.aip.org/content/aip/journal/pop/21/3?ver=pdfcov>

Published by the [AIP Publishing](#)

---

### Articles you may be interested in

[Comparison between kinetic-ballooning-mode-driven turbulence and ion-temperature-gradient-driven turbulence](#)  
*Phys. Plasmas* **21**, 052301 (2014); 10.1063/1.4873379

[Benchmarking gyrokinetic simulations in a toroidal flux-tube](#)  
*Phys. Plasmas* **20**, 092511 (2013); 10.1063/1.4821982

[Ion temperature gradient instability at sub-Larmor radius scales with non-zero ballooning angle](#)  
*Phys. Plasmas* **20**, 022101 (2013); 10.1063/1.4789856

[Gyrokinetic global three-dimensional simulations of linear ion-temperature-gradient modes in Wendelstein 7-X](#)  
*Phys. Plasmas* **11**, 3196 (2004); 10.1063/1.1737393

[Fluid description of electron temperature gradient driven drift modes](#)  
*Phys. Plasmas* **8**, 4340 (2001); 10.1063/1.1386803

---



**AIP** | Journal of  
Applied Physics

*Journal of Applied Physics* is pleased to  
announce **André Anders** as its new Editor-in-Chief

# Finite ballooning angle effects on ion temperature gradient driven mode in gyrokinetic flux tube simulations

Rameswar Singh,<sup>1,2,a)</sup> S. Brunner,<sup>3</sup> R. Ganesh,<sup>1</sup> and F. Jenko<sup>4</sup>

<sup>1</sup>Institute for Plasma Research, Bhat Gandhinagar, Gujarat 2382 428, India

<sup>2</sup>Laboratoire de Physique des Plasmas, Ecole Polytechnique, Route de Saclay, 91128 Palaiseau Cedex, France

<sup>3</sup>CRPP, Ecole Polytechnique Federale de Lausanne, CH-1015 Lausanne, Switzerland

<sup>4</sup>Max-Planck-Institut für Plasmaphysik, EURATOM Association, D-85748 Garching, Germany

(Received 6 December 2013; accepted 3 March 2014; published online 18 March 2014)

This paper presents effects of finite ballooning angles on linear ion temperature gradient (ITG) driven mode and associated heat and momentum flux in Gyrokinetic flux tube simulation GENE. It is found that zero ballooning angle is not always the one at which the linear growth rate is maximum. The ITG mode acquires a short wavelength (SW) branch ( $k_{\perp}\rho_i > 1$ ) when growth rates maximized over all ballooning angles are considered. However, the SW branch disappears on reducing temperature gradient showing characteristics of zero ballooning angle SWITG in case of extremely high temperature gradient. Associated heat flux is even with respect to ballooning angle and maximizes at nonzero ballooning angle while the parallel momentum flux is odd with respect to the ballooning angle. © 2014 AIP Publishing LLC. [<http://dx.doi.org/10.1063/1.4868425>]

## I. INTRODUCTION

Tokamak plasmas are well known to be in turbulent state due to micro scale instabilities from ion to electron Larmor radius scales driven by equilibrium temperature and density gradients. Radially outward lossy transport of different properties (e.g., heat or particle flux) of electron and ions are supposed to happen through distinct channels created by these electron and ion scale micro turbulence. More specifically, radially outward ion heat loss is caused by ion temperature gradient (ITG) driven mode. Among the various approaches, gyrokinetic flux tube simulations are used as first principle calculations to study various properties of these micro instabilities in a tokamak.<sup>1,2</sup> Numerous works have been reported on various aspects of these microinstabilities and microturbulence driven by them. Extensive parametric studies of the linear ITG mode have been carried by many authors over the past years. Flux tube simulations, taking advantage of the short perpendicular wavelength and long parallel wavelength, i.e., ( $k_{\perp} \gg k_{\parallel}$ ) of these microinstabilities, make use of the field aligned coordinate system to reduce computational burden.<sup>3</sup> A flux tube is a curved and sheared box centered around a field line that makes an integral number of poloidal turns around the torus thus sampling the entire flux surface. The equilibrium quantities are Taylor expanded to first order in the perpendicular coordinates around the central field line (or box center). The values and first derivatives of equilibrium quantities, together with the metric coefficients that describe the shaping of the box, are taken to be constant over the perpendicular extent of the box. Only parallel variations are taken into account. Such a local approximation is valid when the radial extent of the box is small compared to the machine size. Profile shearing effects, important when  $\rho^*$  is finite, are not captured in this formulation. Periodic boundary conditions are used in radial

( $x$ ) and binormal ( $y$ ) directions, i.e.,  $f(x + L_x, y, z) = f(x, y, z)$  and  $f(x, y + L_y, z) = f(x, y, z)$ , where  $L_x$  ( $L_y$ ) represents simulation box length in radial (binormal) direction. The box lengths are chosen to be bigger than the correlation lengths of the turbulent fields in the corresponding directions. Such periodic boundary conditions allow us to take Fourier representation for the  $x$  and  $y$  directions. The poloidal angle is used to parameterize the parallel direction  $z$ . The magnetic shear  $\hat{s}$  causes coupling of radial modes and leads to the parallel boundary condition  $f(k_x, k_y, z + L_z) = (-1)^{nN} f(k'_x, k_y, z)$ , where  $k'_x = (m + nN)k_x^{min}$  and  $k_y = mk_y^{min}$  and  $k_x = nk_x^{min}$ ,  $m$  and  $n$  take values  $0, \pm 1, \pm 2, \dots$ , and  $k_{x,y}^{min} = 2\pi/L_{x,y}$ .  $N = 2\pi k_y \hat{s} k_y^{min} / k_x^{min}$  is also an integer. The parallel mode structure is formed by coupling all the  $k_x$  modes for a given  $k_y$  where each Fourier mode ( $k_x, k_y$ ) balloon at poloidal angle  $\theta_k = -k_x/k_y \hat{s}$  called ballooning angle. So a set  $\{k_x\} \equiv \{\dots, -k_x^{min}, 0, +k_x^{min}, \dots\}$  forms mode structure in  $z$  or  $\theta$  that is symmetric about low field side (LFS) mid plane ( $\theta = 0$ ). Shifting each of the elements in  $\{k_x\}$  by some non-zero values rotates the mode structure in  $\theta$  and stationing it away from LFS mid plane. That is a shift in the  $k_x$  values balloons the mode in  $\theta$  at  $\theta_0 = -k_{x,center}/k_y \hat{s}$ , where  $k_{x,center}$  represents the central  $k_x$  mode. This paper explores the effects of finite  $k_{x,center}$  on linear eigenvalues spectrum and associated transports of heat and momentum.

The  $k_y$  spectrum of the eigenvalues differs significantly when  $\theta_0 \neq 0$  from that of the commonly considered case of  $\theta_0 = 0$ . Finite growth rates in the usually stable region ( $k_y > 1$ ) lead to development short wavelength (SW) branch when maximum growth rates in  $\theta_0$  scan are considered. This SWITG branch dies out on reduction of equilibrium temperature gradient. This behavior is similar to SWITG reported by authors<sup>4-7</sup> in the past. The fundamental striking difference between our and past works is that past works considered extremely high temperature gradients ( $R/L_T = 25$  with  $R/L_n = 10$ ), which might be prevalent in pedestal and

<sup>a)</sup>rameswar.singh@lpp.polytechnique.fr

transport barriers, and  $\theta_0 = 0$  whereas our results are for regular temperature gradients but at finite  $\theta_0$ . The SW branch is damped out towards lower temperature gradients but max growth rates still showing marked difference from zero ballooning angle growth rates. Impact of finite  $\theta_0$  on associated heat and parallel momentum flux is discussed.

The paper is organized as follows. Section II contains formulation of the gyrokinetic equations in field aligned coordinates as solved in GENE. Diagnostics used to extract various information are also described in this section. Results of linear flux tube simulations for ITG mode are delineated in Sec. III. Finally, discussion and conclusions are made in Sec. IV.

## II. MODEL EQUATIONS

### A. Formulation

The gyrokinetic formalism limited to the simple scenario of a single ion species, adiabatic electrons, electrostatic perturbations for a large aspect-ratio,  $s - \alpha$  model equilibrium is used in this analysis. In this case, the evolution equation for the ion distribution function  $f_i$  appropriately normalized can be written as<sup>8</sup>

$$\begin{aligned} \frac{\partial f_i}{\partial t} + \left[ \omega_n + \omega_{Ti} \left( v_{\parallel}^2 + \mu B_0 - \frac{3}{2} \right) \right] F_{0i} \frac{\partial \bar{\phi}}{\partial y} \\ + \frac{T_{0i} (\mu \hat{B} + 2v_{\parallel}^2)}{q_i B_0} \left( \mathcal{K}_x \frac{\partial h_i}{\partial x} + \mathcal{K}_y \frac{\partial h_i}{\partial y} \right) \\ + \frac{v_{Ti}}{2} \left[ v_{\parallel}^2 + \mu B_0, h_i \right]_{zv_{\parallel}} + [\bar{\phi}, f_i]_{xy} = D[f_i]. \end{aligned} \quad (1)$$

Here,  $h_i$  is the nonadiabatic part of the distribution function,  $h_i = f_i + q_i F_{0i} \bar{\phi} / T_{0i}$ , where  $q_i$  is ion charge normalized to the elementary charge,  $F_{0i}$  is the background distribution function,  $\bar{\phi}$  is the gyro-averaged electrostatic potential,  $v_{Ti} = \sqrt{2T_{0i}/m_i}$  is the ion thermal velocity,  $T_{0i}$  is the ion temperature (normalized to the electron temperature), and  $m_i$  is the ion mass. The electrons are treated adiabatically, and hence only the distribution functions  $f_i$  are evolved in time. The equilibrium magnetic field is expressed by  $B = B_0 B_{ref}$  where  $B_{ref}$  is the reference magnetic field on the magnetic axis.  $D[f_i]$  is a dissipation term given by  $D[f] = -(a_x \partial_x^4 + a_y \partial_y^4 + a_z \partial_z^4 + a_{v_{\parallel}} \partial_{v_{\parallel}}^4) f_i$  where the coefficients  $a_x$ ,  $a_y$ ,  $a_z$ , and  $a_{v_{\parallel}}$  are adapted depending on the class of the physical problems. Finally, the Poisson brackets are defined by  $[f, g]_{ab} = \partial_a f \partial_b g - \partial_b f \partial_a g$ .

The first linear term contains the effect of the fixed ion density  $\omega_{ni} = L_{ref} / L_n$  and temperature  $\omega_{Ti} = L_{ref} / L_T$  gradients expressed in major radius  $L_{ref} = R$  units. The second linear term describes effects due to magnetic curvature in which  $\mathcal{K}_x$  and  $\mathcal{K}_y$  represent the standard curvature terms

$$\mathcal{K}_x = -\frac{L_{ref} \gamma_2}{B_{ref} \gamma_1} \frac{\partial B_0}{\partial z}, \quad \mathcal{K}_y = -\frac{L_{ref}}{B_{ref}} \left( \frac{\partial B_0}{\partial x} - \frac{\gamma_3}{\gamma_1} \frac{\partial B_0}{\partial z} \right), \quad (2)$$

where  $\gamma_{1,2,3}$  are combinations of metric tensor elements  $g^{ij}$  defined as  $\gamma_1 = g^{xx} g^{yy} - g^{xy} g^{xy}$ ,  $\gamma_2 = g^{xx} g^{yz} - g^{yx} g^{xz}$ ,  $\gamma_3 = g^{xy} g^{yz} - g^{xx} g^{xz}$ . Parallel dynamics involving magnetic

trapping as well as the linear Landau damping effect is contained in the third term. The nonlinear term  $[\bar{\phi}, f_i]$  represents the effect of the self-consistent electric field in the  $E \times B$  drift of charged particles. Since only linear calculations are presented in this paper, the effect of non-linear term is ignored. In local GENE, the distribution function  $f_i$  and the other quantities like the electrostatic potential  $\phi$  are Fourier transformed in the radial  $x$  and binormal directions  $y$ , i.e.,  $\frac{\partial}{\partial x} \rightarrow ik_x$  and  $\frac{\partial}{\partial y} \rightarrow ik_y$ , where  $k$  represents wavenumber. The gyrokinetic Poisson equation is used to determine the self consistent electrostatic field which can be expressed in terms of the Fourier modes as follows:

$$\begin{aligned} \frac{q_i^2 n_{0i}}{T_{0i}} (1 - \Gamma_0(b_j)) \phi_k + n_{0e} (\phi_k - \langle \phi \rangle_{FS}) \\ = q_i \pi B_0 n_{0i} \int J_0(\lambda_j) f_i dv_{\parallel} d\mu. \end{aligned} \quad (3)$$

Here,  $\lambda^2 = 2k_{\perp}^2 \mu / B_0$ ,  $b_i = v_{Ti}^2 / 2\Omega_i$  while  $n_{0e}$  and  $n_{0i}$  are, respectively, the equilibrium electron and ion densities. The functions  $J_0$  and  $\Gamma(b_i) = \exp(-b_i) I_0(b_i)$  are, respectively, the Bessel and the scaled modified Bessel functions of order zero.  $k_{\perp}$  is the perpendicular wave number given as  $k_{\perp}^2 = g^{xx} k_x^2 + 2g^{xy} k_x k_y + g^{yy} k_y^2$ , and  $\Omega_i$  is the ion cyclotron frequency. The angular brackets  $\langle \phi \rangle_{FS}$  denote flux surface average of the electric potential.

The above gyrokinetic Vlasov-Maxwell equation is solved for the analytical  $\hat{s} - \alpha$  geometry in flux tube approximation for which the normalized metric and equilibrium magnetic field are approximated by

$$\begin{aligned} g^{ij} = \begin{pmatrix} 1 & \hat{s}z - \alpha \sin z & 0 \\ \hat{s}z - \alpha \sin z & 1 + (\hat{s}z - \alpha \sin z)^2 & 1/r_0 \\ 0 & 1/r_0 & 1/r_0^2 \end{pmatrix}, \\ B_0 = \frac{1}{1 + \epsilon_t \cos \hat{s}z} \quad \frac{\partial B_0}{\partial z} = B_0^2 \epsilon_t \sin z \quad J = \frac{1}{B_0} \quad \epsilon_t = \frac{r_0}{R}. \end{aligned}$$

This leads to the following curvature terms:

$$\begin{aligned} \hat{\mathcal{K}}_x = -\frac{L_{ref}}{R} \sin z, \\ \hat{\mathcal{K}}_y = -\frac{L_{ref}}{R} (\cos z + \sin z (\hat{s}z - \alpha \sin z)). \end{aligned}$$

In the most of following linear calculations, the MHD parameter  $\alpha = -q^2 R d\beta / dr$  is set to zero. The effect of  $\alpha$  has been discussed separately for eigenvalues only.

### B. Diagnostics

The diagnostics used to obtain results in this paper are described as follows.

#### 1. Eigenvalues

Since all the  $k_x$  grid points are coupled via the parallel boundary condition, the linear eigenvalues are computed as follows:<sup>8</sup>

$$\lambda(k_y) = \frac{\sum_{k_x, z} w(k_x, k_y, z) \lambda(k_x, k_y, z)}{\sum_{k_x, z} w(k_x, k_y, z)} \text{ where } \lambda(k_x, k_y, z) = \ln \left( \frac{\phi(t_n)}{\phi(t_{n-1})} \right) / \Delta t. \quad (4)$$

The result  $\lambda = \gamma + i\omega$  represents the combined growth rate and real frequency of the mode  $k_y$ . The convergence criterion for a given  $k_y$  is that the scatter of  $\lambda(k_x, k_y, z)$  is below a certain, adjustable limit  $c_p$  connected to the precision of the value for  $\lambda$

$$\frac{\sum_{k_x, z} w(k_x, k_y, z) |\lambda(k_x, k_y, z) - \lambda(k_y)|^2}{\sum_{k_x, z} w(k_x, k_y, z)} < c_p. \quad (5)$$

Here,  $c_p = 10^{-3}$  has been taken for all computations. The weight function is taken to be  $w(k_x, k_y, z) = \phi(t_{n-1})$ .

## 2. Mode averaged quantities

Mode averaged quantities such as  $k_\perp^2$  are calculated as follows:

$$\langle k_\perp^2 \rangle(k_y) = \frac{\int dz J(z) \sum_{k_x} k_\perp^2 |\phi(k_x, k_y, z)|^2}{\int dz J(z) \sum_{k_x} |\phi(k_x, k_y, z)|^2}, \quad (6)$$

where  $k_\perp^2 = g^{xx} k_x^2 + 2g^{xy} k_x k_y + g^{yy} k_y^2$ .  $J(z)$  is the Jacobian and  $g^{ij}$  are the metric coefficients.

## 3. Momentum and heat fluxes

The generic structure of any flux  $\Gamma_{AB}$  in terms of its spectral components  $A(\vec{k})$  and  $B(\vec{k})$  is given by

$$\Gamma_{AB}(z) = \langle A(x, y, z) B(x, y, z) \rangle_{xy} = \frac{\int dx dy A(x, y, z) B(x, y, z)}{\int dx dy}, \quad (7)$$

$$= \sum_{k_x, k_y} A(k_x, k_y, z) B(k_x, k_y, z).$$

Summation over  $k_y$  extends over all +ve and -ve  $k_y$  modes while GENE outputs for +ve  $k_y$ 's only. Hence using the complex conjugation properties of Fourier amplitudes (i.e.,  $A^*(\vec{k}) = A(-\vec{k})$ ), the above expression is reduced to the following form which uses only  $k_y \geq 0$ :

$$\Gamma_{AB}(z) = \sum_{k_x} A(k_x, 0, z) B(k_x, 0, z) + 2Re \sum_{k_x} \sum_{k_y > 0} A^*(k_x, k_y, z) B(k_x, k_y, z). \quad (8)$$

Volume averaged fluxes are calculated as follows:

$$\Gamma_{AB} = \frac{\int dz J(z) \Gamma_{AB}(z)}{\int dz J(z)}. \quad (9)$$

Substituting radial  $E \times B$  velocity fluctuation  $v_r$  for  $A$  and parallel momentum density  $mu_{||}$  for  $B$  yields parallel momentum density flux  $\Gamma_{||}$

$$\Gamma_{||}(z) = \langle v_r mu_{||} \rangle. \quad (10)$$

Similarly, ion heat flux is defined as

$$Q_i(z) = \left\langle v_r \left( n_0 \frac{T_{||}}{2} + n_0 T_\perp + \frac{3}{2} n T_{i0} \right) \right\rangle, \quad (11)$$

where  $T_{||}$ ,  $T_\perp$ , and  $n$  represent parallel temperature, perpendicular temperature, and density fluctuations of ion and  $n_0$  and  $T_{i0}$  are equilibrium density and temperature of ions.

## III. RESULTS FROM LINEAR GYROKINETICS

In this section, we present the results from the flux tube simulations using the GENE code for the linear electrostatic ITG mode with adiabatic electron response. Various parameters and reference values are tabulated below. Magnetic shear  $\hat{s} = 1$ , inverse aspect ratio  $\epsilon_t = r_0/R_0 = 0.16$ , major radius  $R_0/L_{ref} = 1$ , safety factor,  $q_0 = 2$ , density gradient  $\omega_n = 3$ , and temperature gradient  $\omega_T = 9$  unless stated otherwise. The reference quantities are  $L_{ref} = R_0 = 1.65$  m,  $B_{ref} = 1$  T,  $Q_{ref} = e = 1.6 e-19$  C,  $m_{ref} = m_i = 3.34 e-27$  kg,  $T_{ref} = T_{e0} = 350$  eV,  $n_{ref} = n_i = 3.5 e + 19 m^{-3}$ ,  $c_{ref} = 129487.19$  m/s, and  $\rho_{ref} = 0.0027029701$  m. We would stress here that the marked difference between the parameters chosen here and the previous works on conventional SWITG is that the latter considered very high temperature and density gradients  $R/L_T = 25$  and  $R/L_n = 10$ .

### A. Eigenvalues

Fig. 1 shows  $kx_{center}$  scan of linear growth rates at different bi-normal wavenumber  $k_y$ . The figure has a couple of features that need explanation. The growth rates are periodic in  $kx_{center}$  or  $\theta_0$  for any  $k_y$ . This is due to the fact that non-zero  $kx_{center}$  shifts the eigenmode away from LFS mid-plane, as shown in Fig. 2, where it sees a different magnetic curvature and hence different growth rate.  $2\pi$  periodicity of curvature term in  $\theta$  or  $z$  leads to  $2\pi k_y \hat{s}$  periodicity of the growth rates in  $kx_{center}$ . Another surprising feature of Fig. 1 is that  $kx_{center} = 0$  is not often the maximum growing mode. Low  $k_y$  modes show maximum growth at  $kx_{center} = 0$  while high  $k_y$  modes show maximum growth rate at  $kx_{center} \neq 0$ . That is high  $k_y$  modes have maximum growth rates when the eigenmode is shifted away from the LFS mid plane. Values of  $kx_{center}$  and ballooning angle  $\theta_0$  corresponding to maximum growth rates, viz.,  $kx_{center, max}$  and  $\theta_{0m}$ , respectively, against  $k_y$  are shown in Fig. 3.

When growth rates maximized over all  $kx_{center}$  or  $\theta_0$  are considered the ITG mode instability window in  $k_y$  broadens way beyond  $k_y > 1$  in the SW regime as shown in Figs. 4 and 5. But the SW branch disappears at lower temperature

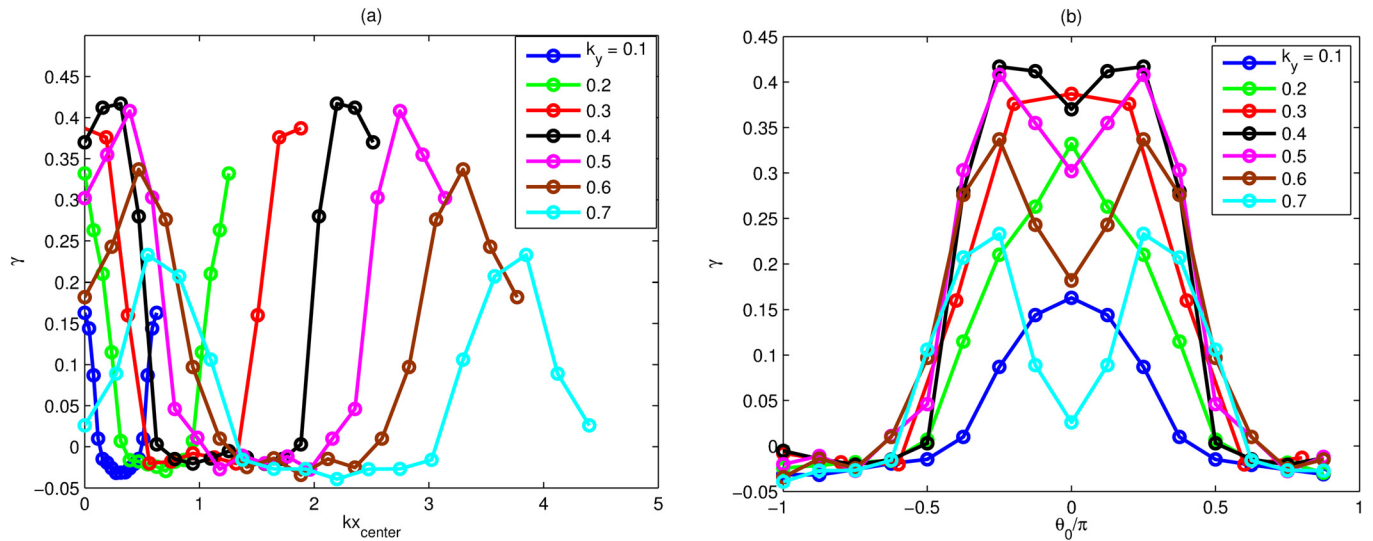


FIG. 1. Linear growth rates  $\gamma$  vs  $kx_{center}$  (a) and  $\gamma$  vs  $\theta_0$  (b) with  $k_y$  as parameter.  $kx_{center}=0$  or  $\theta_0=0$  is not always the maximum growing mode. Very weakly growing modes or damped mode growth rates in the valley are not well converged as per the rule Eq. (5) and are obtained from linear regression analysis of the available time series of  $|n|^2$  and hence are only approximately correct.

gradients. This behavior is similar to  $\theta_0=0$  SWITG driven by extremely large temperature gradients. (In fact, very large density gradient such that diamagnetic frequency exceeds the mode frequency and for  $\eta_i$  to stay above marginality the needed temperature gradient becomes tremendously high. For example, Fig. 10 in Ref. 4 shows that the instability exists for  $R/L_n > 6$  at  $\eta_i = 2.5$  which translates to  $R/L_T > 15$ !) However, the appearance of SW branch in our case, despite having normal temperature gradients, is due to the fact that at high  $k_y$ , the growth rates maximized over all  $\theta_0$ 's are significantly higher than that at  $\theta_0=0$  (Fig. 1).

Toroidicity scan at  $R/L_T=9$  in Fig. 6 shows that mode growth and frequency for  $k_y=0.4$  and  $k_y=1.4$  vanish with decreasing values of toroidicity  $\epsilon_n=L_n/R$ . This confirms that the SW branch is toroidal in nature similar to the low  $k_y$  high wavelength branch. This characteristic of SWITG branch is different from the conventional zero ballooning angle

SWITG which are slab like in nature.<sup>7</sup> Further, it is also interesting to see that the ballooning angle  $\theta_{0m}$  corresponding to maximum growth reduces with toroidicity from  $0.2\pi$  at  $\epsilon_n=1/3$  to 0 at  $\epsilon_n=0.1$  for  $k_y=0.4$ , whereas on the SW side at  $k_y=1.4$  the ballooning angle does not change with toroidicity.

While  $\alpha$  parameter was taken to be 0 in all the above calculations, it can have finite values in real tokamak discharges. Hence effects of finite  $\alpha$  are analyzed. Fig. 7 shows the  $\alpha$  spectrum of growth rates and frequencies at the low and high  $k_y$  peaks for  $R/L_T=9$  in Fig. 4. For  $k_y=0.4$  and  $\theta_0=0$ , the growth rate increases with  $\alpha$  at low values and then decreases beyond  $\alpha > 0.8$  which starts to increase again at very large values beyond  $\alpha > 1.6$ . For the same wavenumber ballooning at  $\theta_0 = \pm 0.2\pi$ , the growth rate peaks at two values of  $\alpha$  near 0 and 1.6. The maximum growth rates increase with  $\alpha$  at low values peaking at around 0.8 and then

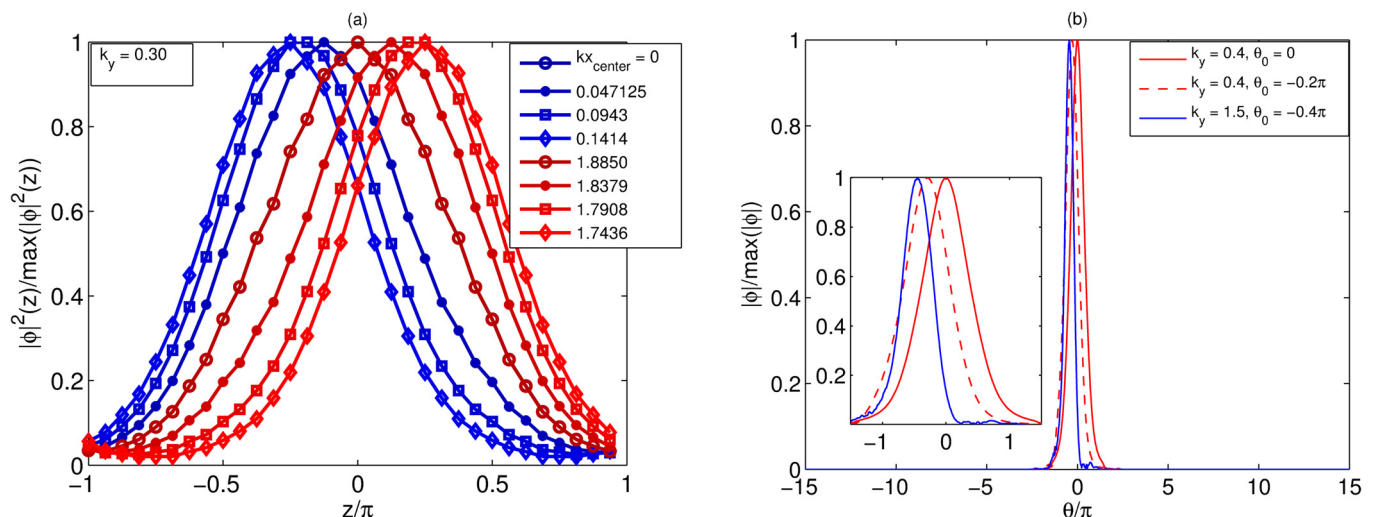


FIG. 2. (a) Finite  $kx_{center}$  shifts mode away from LFS midplane. The figure highlights the same for  $k_y=0.3$  for few representative cases of growing modes. The shown values of  $kx_{center}$  correspond to  $\theta_0/\pi = \{0, -0.05, -0.10, -0.15, 0, 0.05, 0.10, 0.15\}$ . (b) Some typical eigenfunctions in the ballooning space at  $k_y=0.4$  and 1.4. The inset shows zoomed-in plot of the eigenfunctions.

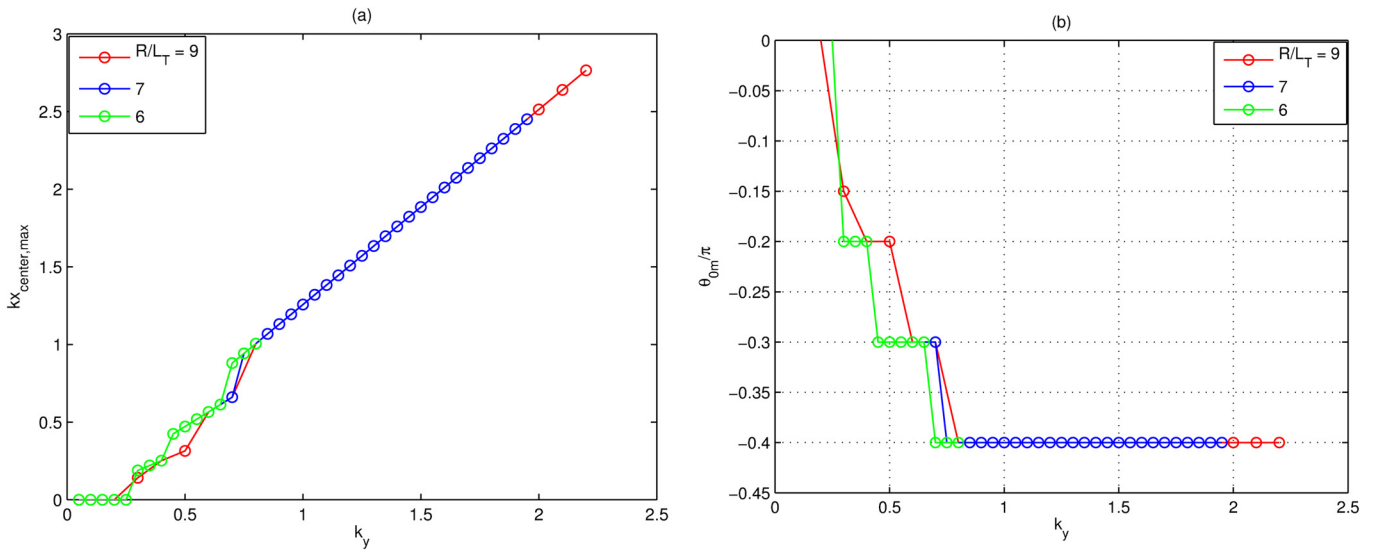


FIG. 3. (a)  $kx_{center}$  vs  $k_y$  at max. growth rates. (b) Ballooning angle  $\theta_{0m}$  at max. growth rate vs  $k_y$ .

decreasing afterwards. At the high  $k_y$  peak for  $R/L_T = 9$ , the growth rate for  $k_y = 1.4$  and ballooning angle  $\theta_0 = 0$  decrease with increasing  $\alpha$  and completely stabilize at  $\alpha = 0.4$ . However, the maximized growth rates show multi-peak characteristic with the height of peaks decreasing with  $\alpha$ . It is also interesting to note that the ballooning angle  $\theta_{0m}$  corresponding to maximum growths decreases from  $0.4\pi$  at  $\alpha = 0$  to 0 at  $\alpha = 1.4$ . The different peaks in the growth rate spectra correspond to different branches as can be seen from jumps in the frequency spectra in Fig. 7(b).

### B. Mixing length estimates

Mixing length estimates are generally used to project estimate of heat diffusivity in nonlinearly saturated turbulence from linear mode calculations. Certainly, these calculations are not full proof but often give an idea of what can be expected in a nonlinearly saturated turbulence regime. Hence, the  $k_y$  spectrum of mixing length estimates for different values of temperature gradient is calculated. Fig. 8 shows

that mixing length values of the SW branch are not much significant compared to the long wavelength part even though estimates due to  $\gamma_{max}$  are higher than that of modes at  $\theta_0 = 0$ . It is important to note that the mixing length spectra peak at  $k_y = 0.1$  in all three cases of  $R/L_T$  and do not show any peak characteristic of SW branch on high  $k_y$  side. The observed monotonically decreasing  $k_y$  spectrum of the mixing length estimates is a consequence of monotonically increasing  $k_y$  spectrum of  $\langle k_{\perp}^2 \rangle$  as shown in the adjoining left figure in Fig. 8.

### C. Momentum and heat fluxes

Parallel momentum density fluxes  $\Gamma_{\parallel}$  normalized by mode intensity  $\langle \phi^2 \rangle$  at  $k_y = 0.3$  as a function of  $\theta_0$  are shown in left panel of Fig. 9.  $\Gamma_{\parallel}/\langle \phi^2 \rangle$  is seen to have odd parity with respect to  $\theta_0$ . This indicates momentum flux reversal with mode tilt angle which may have important implication for understanding of intrinsic toroidal rotation reversal.<sup>9,10</sup> The odd parity of parallel momentum flux is a consequence

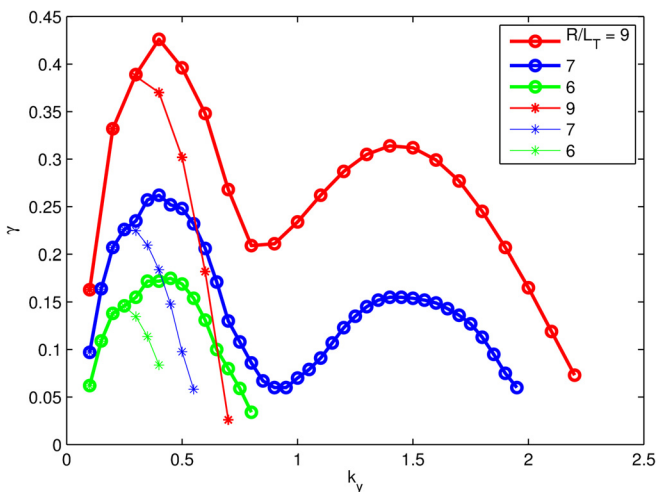


FIG. 4. Thin solid lines with \* indicate  $\gamma$  for  $kx_{center} = 0$ , thick solid lines with o represent  $\gamma$  maximized over all  $kx_{centers}$  i.e.,  $\gamma_{max}$ .

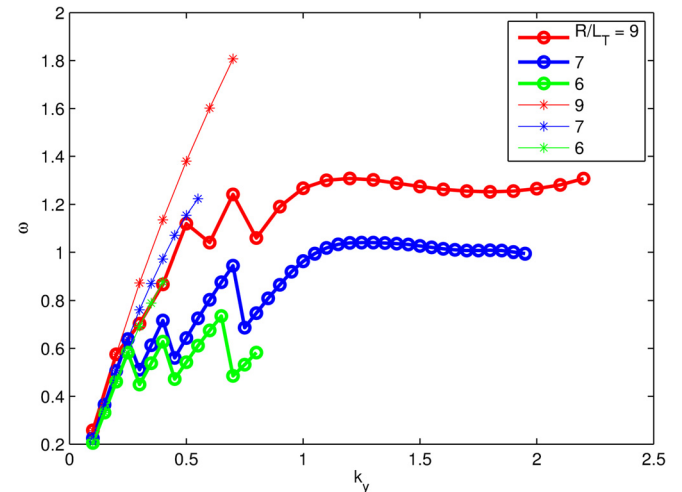


FIG. 5. Thin lines with \* indicate  $\omega$  for  $kx_{center} = 0$ , thick lines with o indicate  $\omega$  corresponding to  $\gamma_{max}$  in Fig. 4.

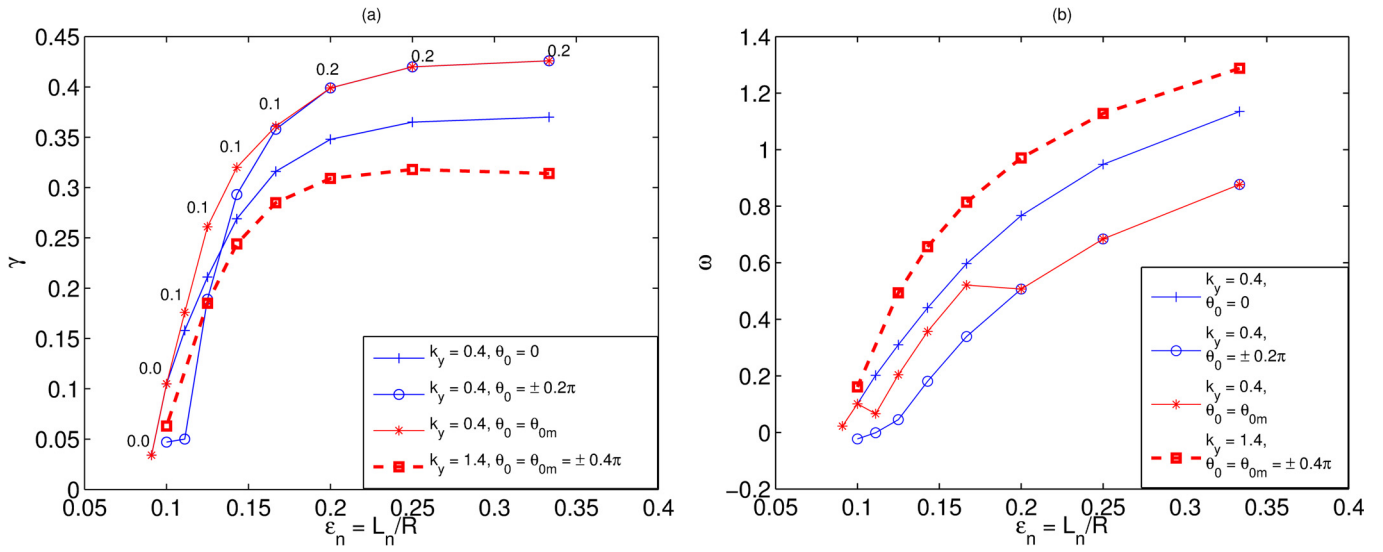


FIG. 6. (a) Growth rates vs toroidicity  $\epsilon_n = L_n/R$  and (b) frequency vs toroidicity  $\epsilon_n = L_n/R$   $k_y = 0.4, 1.4$  and  $R/L_T = 9$ . The numbers indicate values of ballooning angles  $\theta_{0m}$  corresponding to maximum growth.

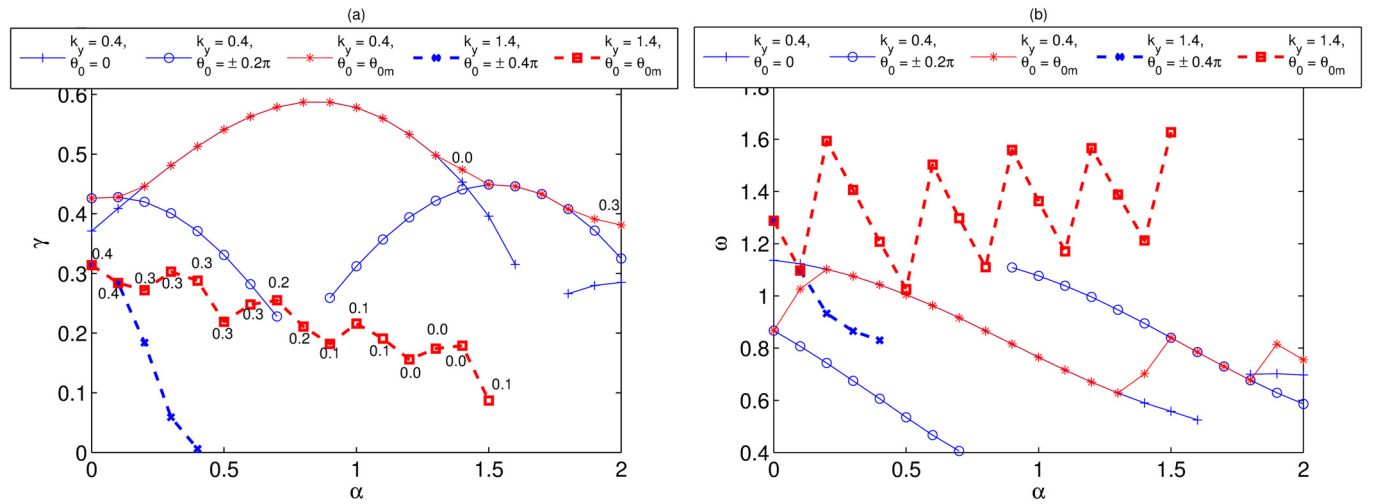


FIG. 7. (a) Growth rates vs  $\alpha$  and (b) frequency vs  $\alpha$  at  $k_y = 0.4, 1.4$  and  $R/L_T = 9$ . The numbers indicate the values of ballooning angles  $\theta_{0m}$  corresponding to maximum growth.

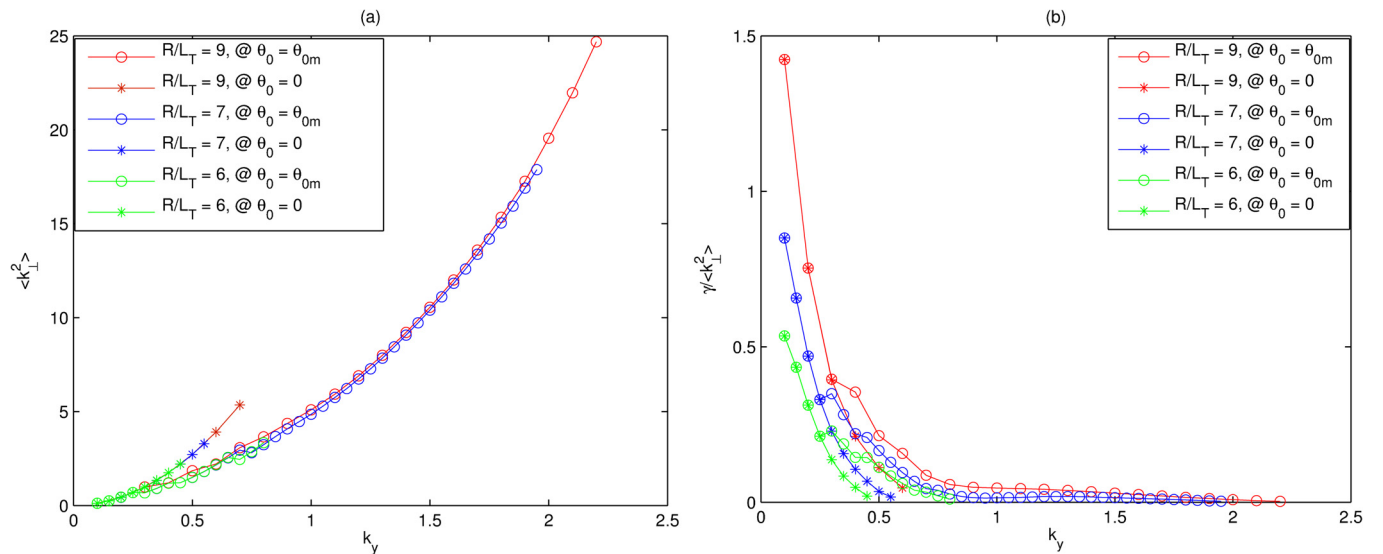


FIG. 8.  $\langle k_\perp^2 \rangle$  vs  $k_y$  (a) and  $\gamma/\langle k_\perp^2 \rangle$  vs  $k_y$  (b) at ballooning angles  $\theta_{0m}$  corresponding to max growth rates  $\gamma_{max}$ .

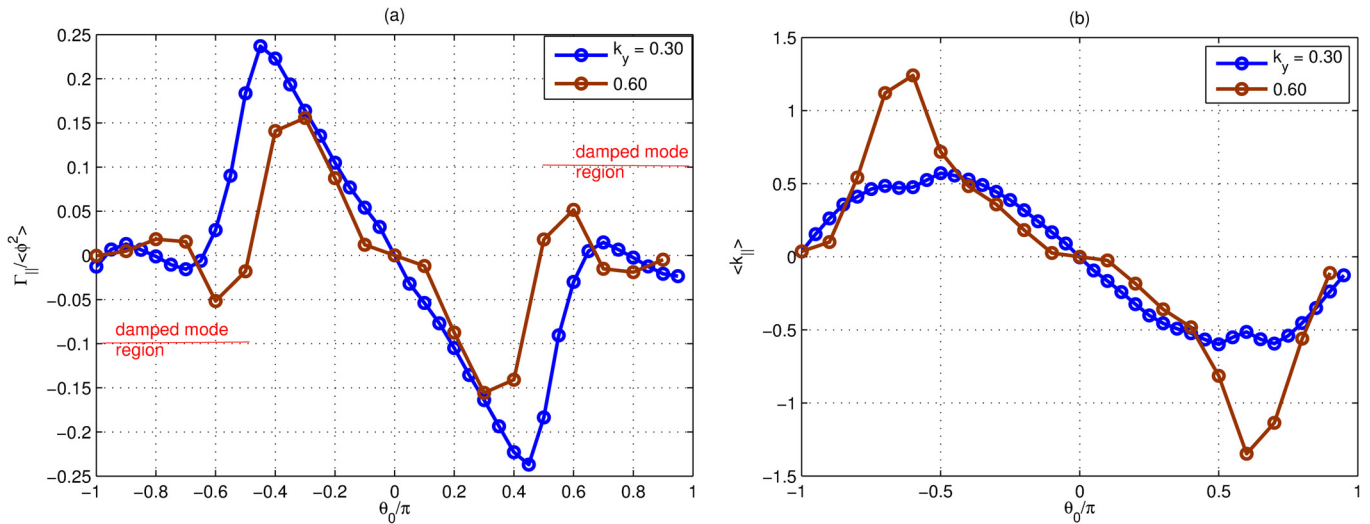


FIG. 9. (a)  $\Gamma_{\parallel}/\langle\phi^2\rangle$  vs  $\theta_0$  at  $k_y = \{0.3, 0.6\}$ ,  $R/L_T = 9$ . The underlined regions indicate damped mode contributions. (b)  $\langle k_{\parallel} \rangle$  vs  $\theta_0$  showing  $\langle k_{\parallel} \rangle$  symmetry breaking by finite  $\theta_0$ .

of odd parity of the eigenmode averaged parallel wavenumber. The right panel of Fig. 9 clearly demonstrates generation of parallel momentum flux due to breaking of  $k_{\parallel}$  symmetry by breaking of eigenmode symmetry caused by finite  $\theta_0$ . The  $k_y$  spectrum of  $\Gamma_{\parallel}$  (unnormalized) exhibits peaks at  $k_y = 0.5$  and  $1.5$  characteristic of long wavelength and short wavelength peaks in growth rate spectra. This is depicted in Fig. 10 for  $\gamma_{max}$ . To nail down, the origin of parallel momentum flux by finite  $\theta_0$   $z$  profiles of  $\Gamma_{\parallel}/\langle\phi^2\rangle$  and mode parities of  $\phi$  and parallel velocity density  $u_{\parallel}$  in  $z$  are calculated. Fig. 11 shows the structure of normalized parallel momentum flux in  $z$  at different values of  $\theta_0$ . It is seen that  $\Gamma_{\parallel}/\langle\phi^2\rangle$  is locally finite but exactly antisymmetric about  $z = 0$  when  $\theta_0 = 0$ . This characteristic can be understood from the even parity of  $\phi$  and odd parity of  $u_{\parallel}$  when  $\theta_0 = 0$  as shown in Fig. 12. In physical words, a mode centered on the LFS mid plane drives parallel momentum flux locally in the poloidal angle but flux in the upper plane is exactly canceled by flux in the lower plane to give no net poloidally averaged parallel

momentum flux. At a finite  $\theta_0$ , the  $z$  profile of  $\Gamma_{\parallel}/\langle\phi^2\rangle$  loses this antisymmetry property in  $z$  hence flux in the upper plane is not exactly canceled by flux in the lower plane constituting a net parallel momentum flux. Again the loss of antisymmetry of  $\Gamma_{\parallel}/\langle\phi^2\rangle$  can be understood from the breaking of symmetry of  $\phi$  and anti-symmetry of  $u_{\parallel}$  about the LFS mid plane (i.e.,  $z = 0$ ) at finite  $\theta_0$  as shown in Fig. 13.

Normalized heat flux  $Q_i/\langle\phi^2\rangle$  exhibits even parity in  $\theta_0$  with a nonzero minimum at  $\theta_0 = 0$ . Fig. 14 shows  $Q_i/\langle\phi^2\rangle$  vs  $\theta_0$  for a test case of  $k_y = 0.3$  and  $R/L_T = 9$ .  $Q_i/\langle\phi^2\rangle$  increases with  $\theta_0$  up to  $\theta_0 = \pm 0.45\pi$  and then decreases rapidly to vanishingly small values as  $\theta_0 \rightarrow \pm\pi$  in the damped eigenmode region. Heat flux distribution in poloidal angle  $z$  is shown for different eigenmode ballooning angles are shown in Fig. 15. Heat flux  $z$  profile is seen to follow the  $z$  profile of mode intensity. Heat flux profile is exactly symmetric about  $z = 0$  when  $\theta_0 = 0$ . At finite  $\theta_0$  eigenmode intensity is shifted either below or above the LFS mid plane depending on its sign which is also reflected in the poloidal

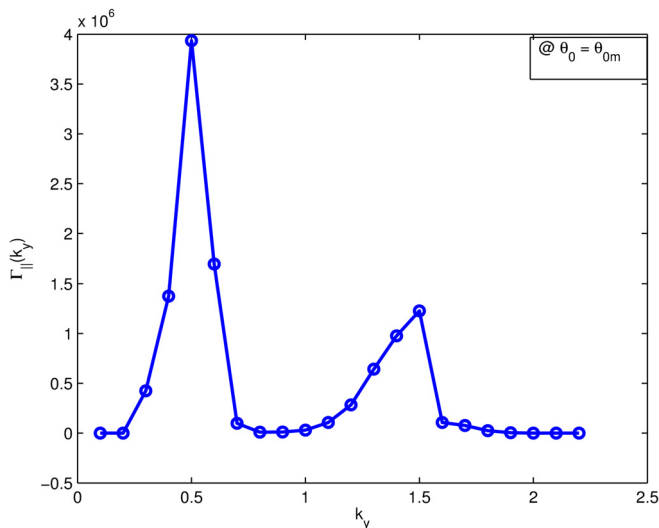


FIG. 10.  $\Gamma_{\parallel}$  vs  $k_y$  at ballooning angles  $\theta_{0m}$  corresponding to max growth rate and  $R/L_T = 9$ .

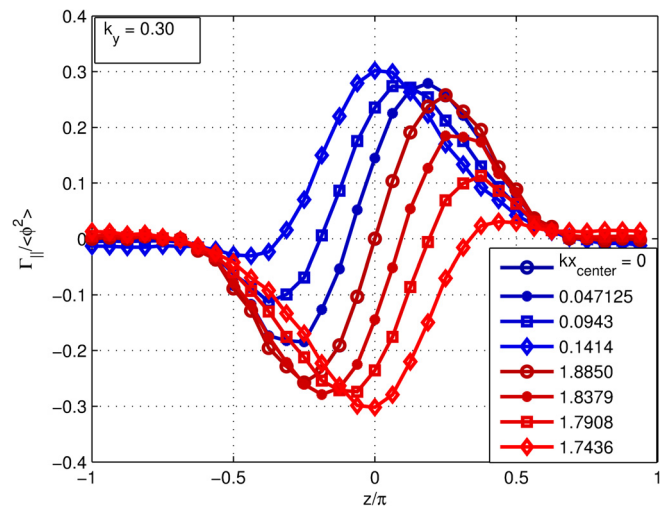


FIG. 11.  $\Gamma_{\parallel}$  vs  $z$  with  $kx_{center}$  as parameter at  $k_y = 0.3$  and  $R/L_T = 9$ . The shown values of  $kx_{center}$  correspond to  $\theta_0/\pi = \{0, -0.05, -0.10, -0.15, 0, 0.05, 0.10, 0.15\}$ .

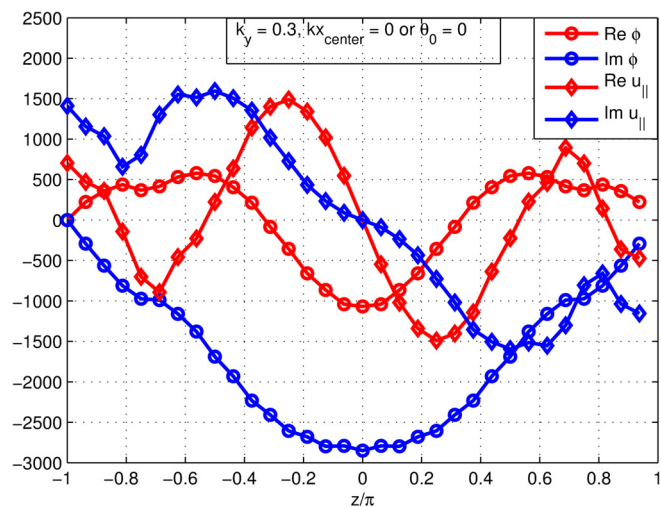


FIG. 12. Mode parities, at the end of simulation, along the field line when  $kx_{center} = 0$  for  $k_y = 0.3$  at  $R/L_T = 9$ .

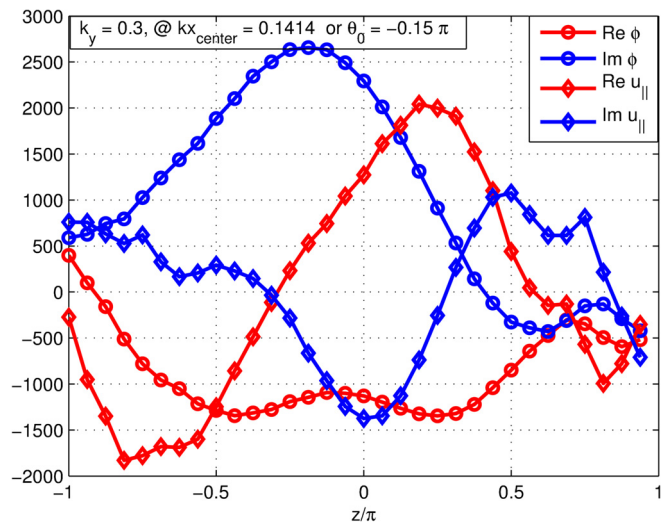


FIG. 13. Mode parities, at the end of simulation, along the field line when  $\theta_0 = -0.15\pi$  for  $k_y = 0.3$  at  $R/L_T = 9$ .

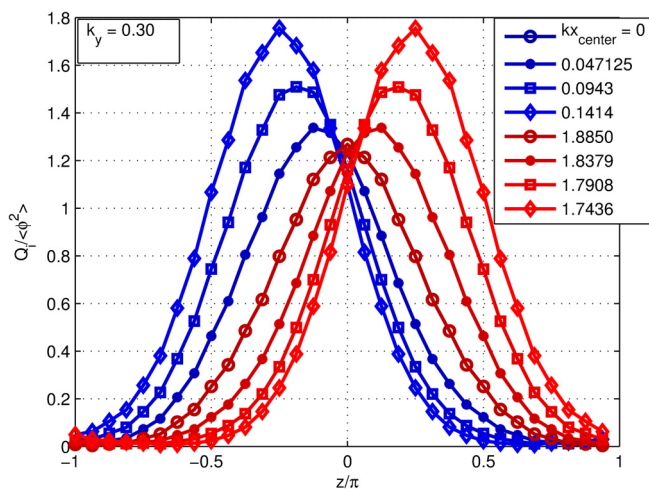


FIG. 15.  $Q_i$  vs  $z$  with  $kx_{center}$  as parameter at  $k_y = 0.3$  and  $R/L_T = 9$ . The shown values of  $kx_{center}$  correspond to  $\theta_0/\pi = \{0, -0.05, -0.10, -0.15, 0, 0.05, 0.10, 0.15\}$ .

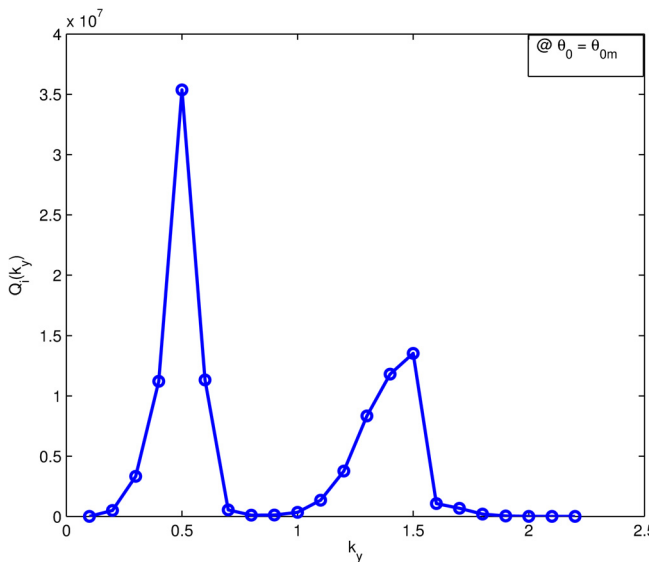


FIG. 16.  $Q_i$  vs  $k_y$  at ballooning angles  $\theta_{0m}$  corresponding to max growth rate and  $R/L_T = 9$ .

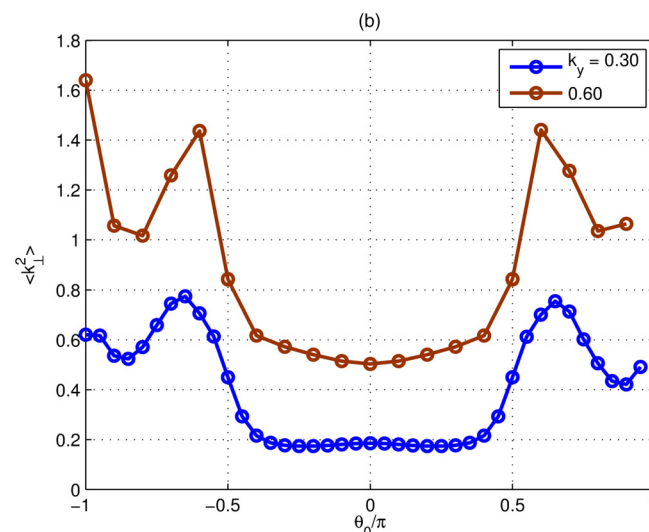
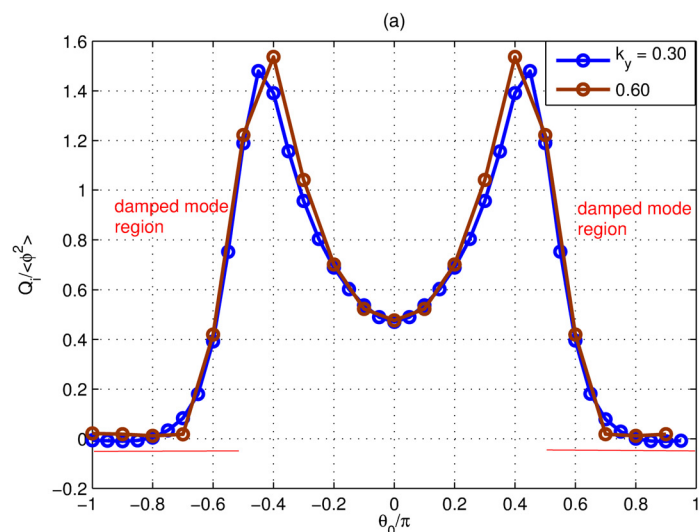


FIG. 14. (a)  $Q_i / \langle \phi^2 \rangle$  vs  $\theta_0$  at  $k_y = \{0.3, 0.6\}$ ,  $R/L_T = 9$ . The underlined regions correspond to damped modes. (b)  $\langle k_{\perp}^2 \rangle$  vs  $\theta_0$ .

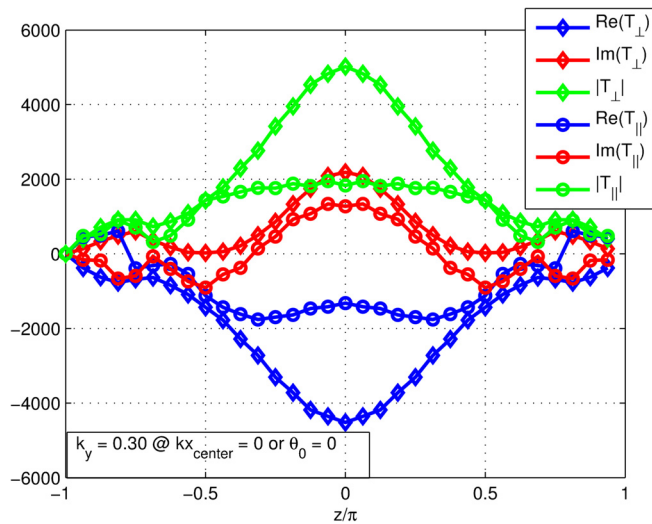


FIG. 17. Mode parities, at the end of simulation, along the field line when  $\theta_0 = 0$  for  $k_y = 0.3$  at  $R/L_T = 9$ .

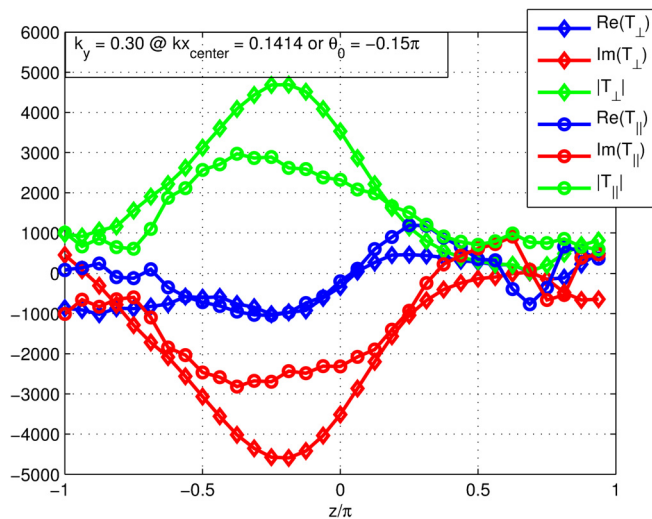


FIG. 18. Mode parities, at the end of simulation, along the field line when  $\theta_0 = -0.15\pi$  for  $k_y = 0.3$  at  $R/L_T = 9$ .

structure of the heat flux. Like  $k_y$  spectrum of parallel momentum flux, the  $k_y$  spectrum of ion heat flux in Fig. 16 shows peaks at  $k_y = 0.5$  and  $1.5$  characteristic of long and short wavelength growth spectra respectively. The even parity of heat flux with respect to  $\theta_0$  could be understood from the fact that potential fluctuation  $\phi$ , parallel temperature fluctuation  $T_{\parallel}$ , and perpendicular temperature fluctuations  $T_{\perp}$  all have same even parity when  $\theta_0 = 0$  as shown in Fig. 17. This symmetry is broken when  $\theta_0 \neq 0$  and the fluctuation intensity in all fields maximizes at position other than  $z = 0$  as shown in Fig. 18 for an example of  $\theta_0 = -0.15\pi$ .

#### IV. DISCUSSION AND CONCLUSIONS

We performed flux tube simulations of linear ITG mode exploiting the freedom of mode ballooning angle for the first time. So far, flux tube simulations have only been reported

for  $\theta_0 = 0$  in the best of our knowledge. Following are the major findings that add to the conventional wisdom:

- High  $k_y$  modes often show maximum growth rates at  $\theta_0$ 's other than 0.
- ITG instability window extends to SW regime  $k_y > 1$  when growth rates maximized over all ballooning angles are considered.
- The SW branch dies out on decreasing  $R/L_T$  showing behavior similar to the zero ballooning angle SWITG driven by extremely large temperature gradients.
- The SW branch is toroidal in nature as opposed to the slab like nature of conventional zero ballooning angle SWITG.
- $\alpha$  has overall stabilizing effect on the SW branch.
- Though mixing length estimates of  $\gamma_{max}$  are slightly greater than that of  $\gamma_0$ , the SW branch shows insignificantly low contribution to mixing length estimates compared to the long wavelength branch.
- Loss of symmetry of potential fluctuation and loss of anti-symmetry of parallel velocity fluctuations about LFS mid plane due to finite  $\theta_0$  lead to net poloidally averaged parallel momentum flux. The parallel momentum flux is anti-symmetric with respect to  $\theta_0$ , which provides a mechanism of flux reversal and hence reversal of intrinsic toroidal rotation.
- Heat flux shows even parity with respect to  $\theta_0$ .
- Un-normalized heat and momentum flux  $k_y$  spectra obtained from  $\gamma_{max}$  modes show peaks at  $k_y = 0.5$  and  $1.5$  characteristic of both low  $k_y$  and high  $k_y$  spectrum of  $\gamma_{max}$ .

The freedom of setting arbitrary  $\theta_0$  deserves some discussion. The periodic nature of growth rates of the eigenmodes with respect to  $\theta_0$  can best be understood by calculating eigenmode averaged curvatures  $\langle \hat{\mathcal{K}}_y \rangle = \int_{-\pi}^{+\pi} dz \hat{\mathcal{K}}_y(z) |\phi|^2(z) / \int_{-\pi}^{+\pi} dz |\phi|^2(z)$ . For a test eigenfunction of the type  $\phi = (1 + \cos(\theta - \theta_0))$ , it is easy to show that  $\langle \hat{\mathcal{K}}_y \rangle$  consists of terms proportional to  $\sin\theta_0$  and  $\cos\theta_0$ . That is an eigenmode ‘‘ballooned’’ at different poloidal angles samples different effective magnetic field curvatures and hence different growth rates periodic in  $\theta_0$  for effective curvature being periodic in  $\theta_0$ . This is shown in an example for  $k_y = 0.6$  in Fig. 19. But understanding of why  $\theta_0 = 0$  modes are not maximum growing modes at high  $k_y$  region requires further deep investigation which is not within the scope of this paper.

Obviously, the freedom of choosing  $\theta_0$  is neither desirable nor self-consistent for the description of the mode. What decides ballooning angle in more realistic situation when global profile effects are considered? Eigenmode ballooning angle becomes a free parameter in flux tube simulations due to Fourier decomposition of perturbations in radial direction allowed by periodic radial boundary condition which is based on assumption that the profile shearing effects are not important, i.e.,  $\rho^* \rightarrow 0$ . Hence, it is natural to wonder if eigenmode ballooning angle in a global calculation with finite  $\rho^*$  corresponds to  $\theta_{0m}$  at all. In conventional ballooning representation/formalism for 2D eigenmode structure calculation in the poloidal plane, the solution of the global eigenmode is accomplished in two steps. In the lowest order in  $1/n$ , where  $n$  is toroidal mode number, the eigenmode structure along the field line is calculated via an eigenvalue

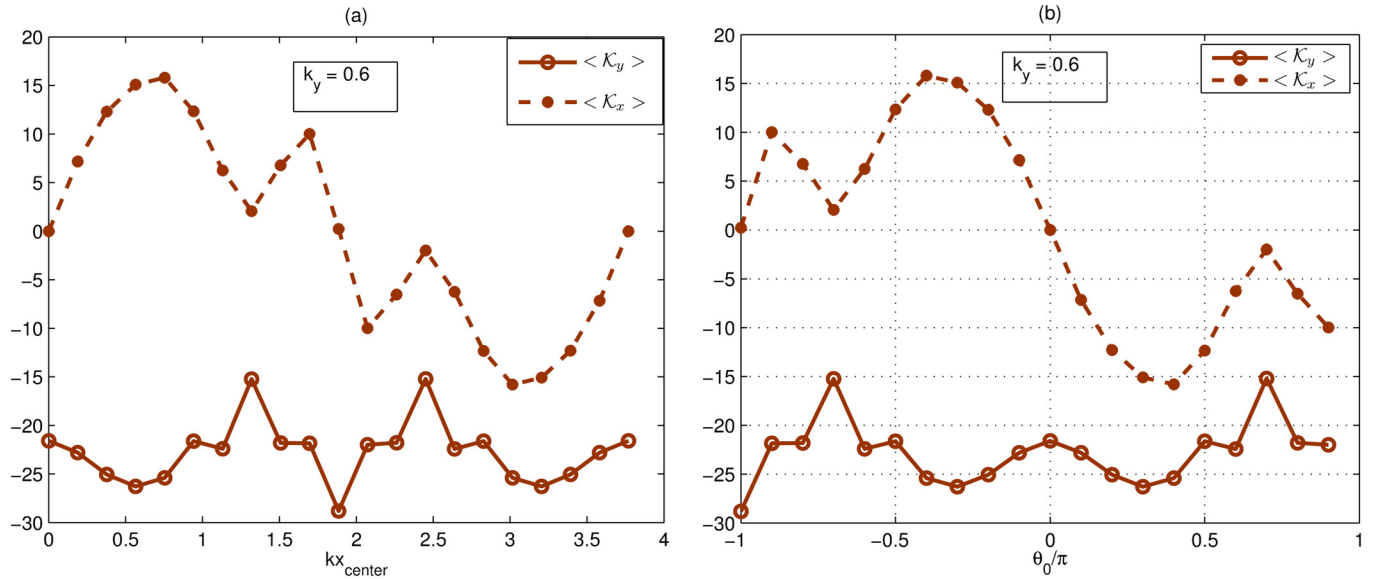


FIG. 19. Eigenmode averaged curvatures  $\langle \mathcal{K}_x \rangle$ ,  $\langle \mathcal{K}_y \rangle$  vs  $kx_{center}$  (a) and  $\theta_0$  (b) for a test case of  $k_y = 0.6$  when  $R/L_T = 9$ . The periodic nature of  $\gamma$  is a reflection of periodic nature of  $\mathcal{K}_y$ .

problem in which  $\theta_k$ , which actually appears as an operator  $\theta_k = -(i/nq') d/dx$ , is set to zero and local approximation to global eigenvalues is obtained.<sup>11</sup>  $\theta_k$  is determined self-consistently from the integrability condition of the next order inhomogeneous radial envelope equation.<sup>12</sup> Kim *et al.*<sup>13</sup> and Kishimoto *et al.*<sup>14,15</sup> showed that in 2D envelope problem, the most unstable mode is characterized by ballooning angle  $\theta_{0m} = -\text{sign}(\hat{s}\omega_r'(\omega_r'/2k_\theta\gamma_0\hat{s})^{1/3})$ , where  $\gamma_0$  is growth rate at zero ballooning angle and  $\omega_r'$  is shear in real frequency due to equilibrium profile shear which is a finite  $\rho^*$  effect. Hence, imposing finite tilts in flux tube simulations seems to violate the basic philosophy of taking  $\rho^* \rightarrow 0$  in the same. A comparison of  $\theta_{0m}$  of the modes reported here with the poloidal tilt angle in global gyrokinetic simulations is desired which is left for future work.

## ACKNOWLEDGMENTS

This work was done during the stay of R. Singh at CRPP, Lausanne under the ISJRF Program 2011-2012 Grant No. RF37. The hospitality provided is greatly acknowledged. The results were obtained with the assistance of high performance computing resources on the HPC-FF systems at Jülich, Germany. R. Singh is extremely thankful to D. Told, T. Goerler, and H. Doerk for fruitful discussions during this work. R. Singh is also thankful to Y. Camenen and A. G. Peeters for occasional discussions. Ö. D. Gürçan and P.

Morrel are greatly acknowledged for their helps in getting further results on Helios in response to the referee comments.

- <sup>1</sup>F. Jenko, W. Dorland, M. Kotschenreuther, and B. N. Rogers, *Phys. Plasmas* **7**, 1904 (2000).
- <sup>2</sup>A. Peeters, Y. Camenen, F. Casson, W. Hornsby, A. Snodin, D. Strintzi, and G. Szepesi, *Comp. Phys. Commun.* **180**, 2650 (2009).
- <sup>3</sup>M. A. Beer, S. C. Cowley, and G. W. Hammett, *Phys. Plasmas* **2**, 2687 (1995).
- <sup>4</sup>J. Chowdhury, R. Ganesh, J. Vaclavik, S. Brunner, L. Villard, and P. Angelino, *Phys. Plasmas* **16**, 082511 (2009).
- <sup>5</sup>Z. Gao, H. Sanuki, K. Itoh, and J. Q. Dong, *Phys. Plasmas* **10**, 2831 (2003).
- <sup>6</sup>Z. Gao, H. Sanuki, K. Itoh, and J. Q. Dong, *Phys. Plasmas* **12**, 022502 (2005).
- <sup>7</sup>A. Hirose, M. Elia, A. I. Smolyakov, and M. Yagi, *Phys. Plasmas* **9**, 1659 (2002).
- <sup>8</sup>F. Merz, "Gyrokinetic simulation of multimode plasma turbulence," Ph.D. thesis, der Westfälischen Wilhelms-Universität Münster, 2010.
- <sup>9</sup>Y. Camenen, Y. Idomura, S. Jolliet, and A. Peeters, *Nucl. Fusion* **51**, 073039 (2011).
- <sup>10</sup>A. Bortolon, B. P. Duval, A. Pochelon, and A. Scarabosio, *Phys. Rev. Lett.* **97**, 235003 (2006).
- <sup>11</sup>F. Romaneli and F. Zonca, *Phys. Fluids B* **5**, 4081 (1993).
- <sup>12</sup>R. J. Hastie, K. W. Hesketh, and J. B. Taylor, *Nucl. Fusion* **19**, 1223 (1979).
- <sup>13</sup>J. Y. Kim, Y. Kishimoto, M. Wakatani, and T. Tajima, *Phys. Plasmas* **3**, 3689 (1996).
- <sup>14</sup>Y. Kishimoto, J. Y. Kim, W. Horton, T. Tajima, M. J. LeBrun, and S. Shirai, *Plasma Phys. Control. Fusion* **40**, A663 (1998).
- <sup>15</sup>Y. Kishimoto, J. Y. Kim, W. Horton, T. Tajima, M. J. LeBrun, S. A. Dettrick, J. Q. Li, and H. Shirai, *Nucl. Fusion* **41**, A663 (1999).